38th AIAA Thermophysics Conference
6-9 June 2005, Toronto, Ontario Canada

AIAA 2005-5325

Laser Absorption Spectroscopy in High Enthalpy Flows

Makoto Matsui* and Kimiya Komurasaki†
The University of Tokyo, Chiba 277-8583, Japan

and

Yoshihiro Arakawa‡
The University of Tokyo, Tokyo 113-8656, Japan

Laser Absorption Spectroscopy has been developed as a diagnostics tool for high enthalpy flow. Firstly an applicable limit of this system was investigated considering error analysis and an influence of absorption saturation. Then this system was applied to two kinds of plasma wind tunnels flows. As a result, in arc-heater plumes, oxygen injected at the constrictor was found not enough mixed with argon base flow at the nozzle exit. The oxygen slowly diffused toward the axis in the downstream region of the plume, resulting in the quite small degree of dissociation of oxygen at the level of 0.01%. In IPG3 plume, the averaged degree of dissociation of oxygen was found to be more than 0.92. The total enthalpy was estimated as 33.7±2.9 MJ/kg; 43% of it was possessed as the chemical potential. These results show good agreement with intrusive measurements.

I. Introduction

When spacecraft entry atmosphere of the earth or other planets, their entry velocity will be several km/s and then they are exposed to severe heat loads by aerodynamic heating [1~5]. Space shuttle entries the earth at the velocity of 7 km/s (Mach >20) and gas temperature in front of its nose is heated up to 7000K. Then, Thermal Protection System (TPS) are essential to protect spacecraft from such severe conditions.

However, unfortunately, there is no facility to simulate such severe reentry conditions completely. Then various types of ground test facilities have been developed to simulate specific conditions [1]. Although, ballistic range, shock tubes, expansion tubes and shock tunnels (including reflected shock tunnels, gun tunnels, Stalker tubes) can produce high temperature and high total pressure conditions, their run time is restricted to be several μs to ms. It is too short for TPS tests because TPS surfaces remains cold and may less interact with the hot gas than actual flight conditions. The short run time also complicates measurement techniques. Therefore, plasma wind tunnels that can produce high temperature conditions for more than several ten minutes are most suitable for TPS tests and widely used in the world [6-8].

Since 1950's, various plasma wind tunnels have been developed for various operational conditions. According to Smith [9], these wind tunnels are classified into six types with respect to their heating methods: Huels arc, constricted arc, magnetically stabilized, segmented arc, magnetoplasmadynamic (MPD) and inductively coupled plasma (ICP). In this research, constricted arc and ICP wind tunnels were targeted. A constricted arc wind tunnel has advantages of simple and rugged structure, long test time and relatively ease of maintenance. On the other hand, an ICP wind tunnel has advantages of low contamination of flow and use of reactive gas due to electrode-less heating.

For evaluation of TPS performances, it is necessary to characterize high enthalpy flows generated by plasma wind tunnels. However their exact plume conditions are mostly unknown because they are usually in strong thermo-chemical non-equilibrium. Although non-intrusive spectroscopic methods such as emission spectroscopy and Laser Induced Florescence have been actively applied to the characterization of such high enthalpy plumes, and the excitation, vibration, and rotational temperatures of atoms and molecules in the plumes are gradually clarified, [10-13] it is still difficult to measure the chemical compositions by these spectroscopic methods. Especially mechanisms of catalytic effects and oxidation of TPS, which have been recognized to cause heat flux enhancement and TPS damage,

* JSPS Research Fellow, Department of Advanced Energy; matsui@al.t.u-tokyo.ac.jp. Member AIAA.
† Associate Professor, Department of Advanced Energy. Member AIAA.
‡ Professor, Department of Aeronautics and Astronautics. Member AIAA.

have not been enough clarified resulting in that TPS has been designed with a large factor of safety [14-17]. Then, accurate characterization of flows makes it possible to reduce TPS weight. Moreover, the characterization is useful for validations of CFD calculations for non-equilibrium flows.

In this research, laser absorption spectroscopy (LAS) was adopted as a diagnostics tool. It is much superior to conventional probe methods: 1) it doesn't disturb flows 2) translational temperature and number density can be measured though they are difficult to be measured by probe methods [18-20]. Furthermore, compared with other spectroscopy such as emission spectroscopy (ES) and LIF, LAS has following advantages as follows.

It can be possible for optically thick plasma and number density can be obtained without calibration though others are not applicable to such plasma and need an absolute calibration source or a reference cell. Furthermore, using a diode laser, whole system is very low cost and compact. Then, the system can be portable everywhere. On the other hand, monochromator or excimer and dye lasers are expensive. Especially the excimer laser is a large equipment and almost impossible to carry. As for the wavelength resolution, in LAS around 0.001nm is possible using etalon whereas that of monochromater is around than 0.1nm.

Objectives of this research are 1) to establish a diagnostic system for two kinds of plasma wind tunnels using diode laser absorption spectroscopy and 2) to characterize flow properties in low-pressure plasma wind tunnel.

Table 1. Comparison of spectroscopes.

	LAS	ES	LIF
Optically thick plasma	Applicable	Inapplicable	Inapplicable
Calibration	No need	Absolute light source	Reference cell
Portability	Easy	Possible	Impossible
Equipment	Not expensive	Expensive	Very expensive
Wave-length resolution	<1pm	~0.1nm	<1pm

II. Laser Absorption Spectroscopy

From the quantum theory [21], of the infinite number of orbits of an electron about an atomic nucleus, which are possible according to classical mechanics, only certain discrete orbits actually occur. A transition of the electron from one state to another can take place by absorbing a incident laser beam whose energy corresponds to the difference between the two states. This absorption profile of atomic lines has information such as its wavelength, intensity and shape. From such information, number density, translational temperature and flow velocity of the absorbing atom can be deduced.

A. Principle of Laser Absorption Spectroscopy [18]

1. Absorption Coeffcient

The relationship between probe laser intensity I and absorption coefficient $k(x)$ is expressed by the Beer-Lambert law as,

$$\frac{\mathrm{d}I}{\mathrm{d}x} = -k(x)I \,. \tag{1}$$

Here, x is the coordinate in the laser pass direction. Because distributions of absorption properties in plumes would be axisymmetric, local absorption coefficient $k_v(r)$ with the radial coordinate r is obtained by the Abel inversion expressed as,

$$k(r) = \frac{1}{\pi}\int_r^R \frac{d(\ln\frac{I}{I_0}(y))}{dy}\frac{dy}{\sqrt{y^2 - r^2}} \,. \tag{2}$$

Here, I_0 is the laser intensity without absorption, y is the beam position and R is the plume radius.

Assuming Boltzmann relation between absorbing and excited states, integrated absorption coefficient $K(r)$ is expressed as a function of the number density at the absorbing state $n_i(r)$ as,

$$K(r)=\int_{-\infty}^{\infty}k_{\nu}(r)\mathrm{d}\nu=\frac{\lambda^2}{8\pi}\frac{g_j}{g_i}A_{ji}n_i(r)\left[1-\exp\left(-\frac{\Delta E_{ij}}{k_{\mathrm{B}}T_{\mathrm{ex}}}\right)\right]. \tag{3}$$

Here, subscripts '*i*' and '*j*' denote the absorbing and excited states, respectively. λ, *g*, *A*, Δ*E*, *k* and T_{ex} are the absorption wavelength, statistical weight, Einstein coefficient, energy gap between the states, Boltzmann constant and electronic excitation temperature, respectively. If $\Delta E_{ij}/kT_{ex}$ is enough large, stimulated emission can be neglected and Eq.(3) is approximated as,

$$K(r)=\frac{\lambda^2}{8\pi}\frac{g_j}{g_i}A_{ji}n_i(r)\,. \tag{4}$$

2. Line Broadening

Absorption profile of atomic line is broadened by various physical mechanisms, and is expressed by a convolution of the Lorentz and the Gauss distributions. Here brief derivations and results are presented [73].

Doppler broadening

The proper frequency ν_0 of a moving atom at velocity v is observed to be shifted by the Doppler effect resulting in causing broadening of the profile. This is called the Doppler broadening. This broadening is a Gauss distribution and its full width at half maximum (FWHM) $\Delta\nu_D$ is related to the translational temperature *T* as,

$$\Delta\nu_D=\frac{2\nu_0\sqrt{\ln 2}}{c}\sqrt{\frac{2k_{\mathrm{B}}T}{M_A}}\,. \tag{5}$$

Here, *c* and M_A are velocity of light and atomic mass.

Natural Broadening

Natural broadening $\Delta\nu_N$ is originated by the finite time of the transition. The uncertainty of the frequency $\Delta\nu_N$ is expressed as,

$$\Delta\nu_{\mathrm{N}}=\frac{A}{2\pi}\,. \tag{6}$$

This broadening is a Lorentz distribution. Generally, typical Einstein constant *A* is from 10^7~$10^8 s^{-1}$ [111]. Then $\Delta\nu_N$ is the order of 2~20 MHz.

Collision Broadening

The collision broadening is originated from the fact that atoms are perturbed by collisions with other atoms (or molecules). This broadening is a Lorentz distribution and its width $\Delta\nu_C$ is expressed as,

$$\Delta\nu_C=\left(C_1+C_2+2C_{12}\right)p \tag{7}$$

Here, *p* is the pressure, C_1, C_2 are the parameters related to with the collision-induced transition, and C_{12} is the parameter related to the phase-changing collision. Values of these three parameters are experimentally found in the range from 1 to 30 MHz/torr depending on the kind of atoms (or molecules) and temperature.

Stark Broadening

Stark broadening originates from the fact that the degeneracy is solved by the electric field which a surrounding electron makes. This broadening is a Lorentz distribution and its width $\Delta\nu_{Stark}$ is expressed as [22],

$$\Delta\nu_{\mathrm{Stark}}=1.0\times\left[1+1.75\times10^{-4}n_{\mathrm{e}}^{1/4}\alpha\left(1-0.068n_{\mathrm{e}}^{1/6}T_{\mathrm{e}}^{-1/2}\right)\right]n_{\mathrm{e}}w10^5 \tag{8}$$

Here, *w* is electron impact parameter, α is ion-broadening parameter, n_e is electron density, and T_e is electron temperature. In case that n_e and T_e are 10^{20} m^{-3} and 10000K, $\Delta\nu_{Stark}$ of OI 777.19 nm is about 33 MHz.

Saturation Broadening

Saturation broadening is originated from the increase in the line width with the optical field intensity. This broadening is a Lorentz distribution and its width $\Delta\nu_{SL}$ at the probe laser intensity I is expressed as,

$$\Delta\nu_{SL} = \Delta\nu_L \sqrt{1 + I / I_{S\_inhomo}} \,. \tag{9}$$

$$I_{S\_inhomo} = \frac{2\pi^2 h \nu^3 \Delta\nu_L}{\phi c^2} \,. \tag{10}$$

Here, $\Delta\nu_L$ is the unsaturated Lorentz width and I_{S_inhomo} is the saturation intensity. However, absorption saturation was found to cause the more broadening than that described above. A detail is described in section Ⅲ.

Transit-time Broadening

Transit-time broadening is originated from the transit of the particles through light beam. This broadening is a Lorentz distribution and its width $\Delta\nu_T$ at the probe laser diameter a is expressed as,

$$\Delta\nu_T = \frac{v}{2\pi a} \,. \tag{11}$$

In case that v and a are 2000 m/s and 1 mm, $\Delta\nu_T$ is about 0.3 MHz.

3. Line Shape Function

The actual absorption profile would be the convolution of the Gaussian and Lorentzian. The profile is called the Voigt profile and expressed as,

$$k(\nu) = \frac{A_{ji} c^2 \Delta\nu_L}{16\pi^2 \nu^2} \left(\frac{g_j}{g_i} n_i - n_j \right) \int_{-\infty}^{\infty} \frac{\exp[-\{2(\nu_\xi - \nu_0)/\Delta\nu_D\}^2 \ln 2] \mathrm{d}\nu_\xi}{(\nu - \nu_\xi)^2 + (\Delta\nu_L/2)^2} \,. \tag{12}$$

Here, ξ represents respective distinguishable part of Lorentz part.

In low-pressure plasma where Doppler broadening is dominant (Voigt parameter $\alpha=(\ln 2)^{1/2}\Delta\nu_L/\Delta\nu_D \ll 1$), the exponential part in Eq. (12) is approximately pulled outside the integrand. The integral is calculated as,

$$k(\nu) = K \frac{2}{\Delta\nu_D} \sqrt{\frac{\ln 2}{\pi}} \exp\left[-\ln 2 \left\{ \frac{2(\nu - \nu_0)}{\Delta\nu_D} \right\}^2 \right] . \tag{13}$$

Then, K and $\Delta\nu_D$ are obtained by a Gauss fitting.

B. Experimental Apparatus

Figure 1 shows a schematic of the measurement system. A tunable diode-laser with an external cavity (Velocity Model 6300; New Focus Inc.) was used as the laser oscillator. Its line width was less than 300 kHz. The laser frequency was scanned over the absorption line shape $k(\nu)$. The modulation frequency and width were 1 Hz and 30 GHz, respectively. An optical isolator was used to prevent the reflected laser beam from returning into the external cavity. An etalon was used as a wave-meter. Its free spectral range was 1 GHz.

The probe beam was guided to the chamber window through a multimode optical fiber. The fiber output was mounted on a one-dimensional traverse stage to scan the flow in the radial direction. The probe beam diameter was 2 mm at

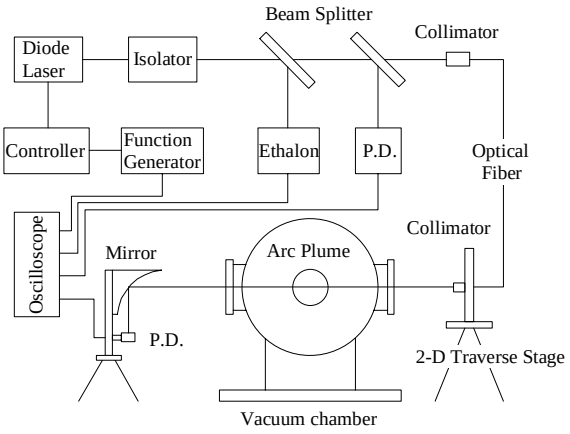

Figure 1. Measurement System.

the chamber center. A parabola mirror allowed scanning of the plume without synchronizing a photo detector (DET110/M; Thorlabs Inc.) position with the probe beam position.

C. Target Lines

In this research, the target absorption lines are the transition from the metastabe oxygen ($3s^5S$) and argon ($4s^2[1/2]$). This is because number density of metastable states is much larger than other excited states one, so that it is easy to detect the absorption profiles. The transition data of these lines and their Grotrian diagrams are shown in Table 2 [23].

Table 2 Transition data.

	i	j	λ, nm	E_i, eV	E_j, eV	g_i	g_j	$A_{ji}, 10^8 s^{-1}$
OI	$3s^5S$	$3p^5P$	777.19	9.15	10.74	5	7	0.369
ArI	$4s^2[1/2]$	$4p^2[3/2]$	840.82	11.62	13.09	3	5	0.223
ArI	$4s^2[3/2]$	$4s^2[5/2]$	842.46	13.28	14.74	3	5	0.215
ArI	$4s^2[1/2]$	$4s^2[3/2]$	852.14	11.62	13.28	3	3	0.139

III. Applicable Limit of Laser Absorption Spectroscopy

In this section, applicable limit of LAS and an effect of laser intensity on translational temperature measurements are investigated. Firstly, errors of absorption coefficients and temperature measurements are analytically discussed and applicable limit of LAS is represented. Secondary, an influence of laser intensity on Doppler broadening is investigated using glow and microwave discharge tube plasma and new broadening model is presented.

A. Error and Applicable Limit of LAS

1. Error of Absorption Coefficient

From Beer-Lambert law Eq. (1), error of absorption coefficient is related to that of fractional absorption expressed as,

$$\frac{\Delta k}{k} = \frac{\Delta\left(I / I_0\right)}{\left(I / I_0\right)\ln\left(I / I_0\right)}. \tag{14}$$

Here, Δk, $\Delta(I/I_0)$ are errors of absorption coefficient and measurement, respectively. Figure 2 shows the estimated error of absorption coefficient for various measurement errors. The error rapidly increases with lower $(I_0\text{-}I)/I_0 < 0.1$. At high $(I_0\text{-}I)/I_0 > 0.99$, the error also increases with $(I_0\text{-}I)/I_0$. However, for high number density states, corresponding errors may be reduced by targeting other degenerate states or higher excited states. Therefore, errors at higher $(I_0\text{-}I)/I_0$ are not discussed below. The fractional absorption more than 1% is measured within 1% error at $\Delta(I/I_0)$ of 10^{-2} %.

2. Error of Temperature

A relationship between errors of absorption coefficient and FWHM is expressed as,

$$\frac{\Delta\left(\Delta\nu_{\mathrm{D}}\right)}{\Delta\nu_{\mathrm{D}}} \approx \frac{\Delta k}{k}. \tag{15}$$

Since FWHM of absorption profiles is calibrated by etalon, its error should be added. Then, the error of width is rewritten as,

$$\frac{\Delta\left(\Delta\nu_{\mathrm{D}}\right)}{\Delta\nu_{\mathrm{D}}} \approx \frac{\Delta k}{k} + \frac{\Delta\mathrm{FSR}}{\Delta\nu_{\mathrm{D}}}. \tag{16}$$

Here, ΔFSR is the etalon error. Assuming the calibration error is 1 %, ΔFSR for FSR of 1GHz is 0.01 GHz.

As shown in Eq. (5), temperature is proportional to the square of FWHM. Then from Eq. (15) temperature error is expressed as,

$$\frac{\Delta T}{T} = 2\frac{\Delta(\Delta\nu_D)}{\Delta\nu_D} \approx 2\left(\frac{\Delta(I/I_0)}{(I/I_0)\ln(I/I_0)} + \Delta\mathrm{FSR}\right). \tag{17}$$

Figure 3 shows temperature errors for $(I_0\text{-}I)/I_0$ >10^{-3} % and T of 500 K and 5000 K. Here, number density corresponding $(I_0\text{-}I)/I_0$ is roughly calculated in which absorption length is set to be 1 cm and λ, A and g in OI 777.19 nm line are used, respectively. With $\Delta(I/I_0)$ of 0.01%, translational temperature is measured with in 5 % error for $(I_0\text{-}I)/I_0$ >10^{-2}. Then, in this case, measurable minimum number density is about 10^{15} m^{-3}.

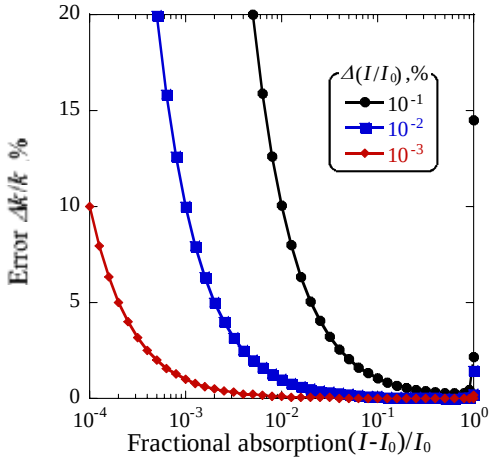

Figure 2. Estimated error of absorption coefficient

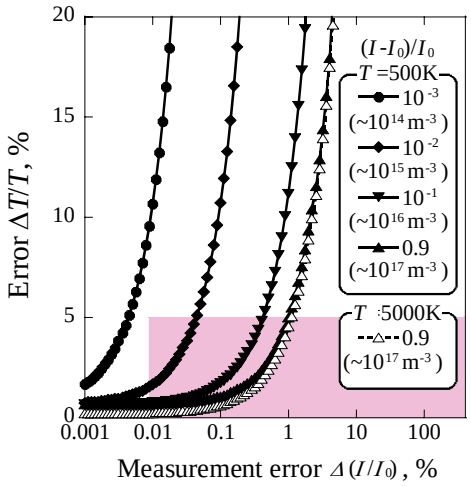

Figure 3. Estimated error of temperature for various fractional absorption and corresponding number density (λ, A, g, are used in OI 777.19nm, absorption length is 1cm.)

B. Influence of Absorption Saturation on Temperature Measurement [24, 25]

1. *Absorption Saturation*

As seen in Eqs. (9, 12, 13), absorption coefficient in low-pressure plasma $k_S(\nu)$ is approximated as,

$$\begin{aligned} k_S(\nu) &= \frac{A_{ji}c^2\Delta\nu_L}{16\pi^2\nu^2}\left(\frac{g_j}{g_i}n_i - n_j\right)\int_{-\infty}^{\infty}\frac{\exp[-\{2(\nu_\xi-\nu_0)/\Delta\nu_D\}^2\ln 2]\,\mathrm{d}\nu_\xi}{(\nu-\nu_\xi)^2+(\Delta\nu_{SL}/2)^2} \\ &= K_0\cdot\frac{2}{\Delta\nu_D}\sqrt{\frac{\ln 2}{\pi}}\exp\left[-\ln 2\left\{\frac{2(\nu-\nu_0)}{\Delta\nu_D}\right\}^2\right]\cdot\left[1+\frac{I}{I_{S\_inhomo}}\right]^{-1/2} \end{aligned}. \tag{18}$$

When pressure broadening is the most dominant in homogeneous broadening, Eq.(10) is rewritten as,

$$I_{S\_inhomo} = \frac{2\pi^2 h\nu^3 N\bar{v}\sigma}{\phi c^2}. \tag{19}$$

Here, N and σ represent the number density of colliding particle and collision cross-section, respectively. $\bar{v}$ is the averaged velocity of absorbers defined as ,

$$\overline{v} = \sqrt{3k_B T / m}\,. \tag{20}$$

If variation of I_{S_inhomo} is very small in the range of $|\nu-\nu_0|<\Delta\nu_D$, Doppler width of the saturated profile $\Delta\nu_{SD}$ is invariant for the variation of laser intensity:

$$\Delta\nu_{SD} = \Delta\nu_D\,. \tag{21}$$

2. Experimental Apparatus

In this study, the influence of laser intensity on broadenings was measured in two types of argon plasma. One is glow discharge tube plasma (CI TECHNO CO., Ltd) whose input power, discharge voltage and ambient pressure were 1.5 W, 4.00 V, and 79 Pa, respectively. This is direct current plasma and the gas is static. The other is TE_{10} mode microwave discharge tube plasma (NIHON KOSHUHA CO., Ltd) whose input power, oscillation frequency, mass flow rate and ambient pressure are 500 W, 2.4 GHz, 20 sccm and 20 Pa, respectively.

In addition to the basic set up described in section Ⅱ, neutral density filters and lenses are used to vary laser intensity. At the measurement points, the laser intensity is ragend from 0.60 mW/mm2 to 2.4.4 mW/mm^2. Target absorption lines are 840.82 nm, 842.46 nm, and 852.14 nm of ArI.

3. Experimental results

Figure 4 shows the measured absorption profiles at 842.46 nm line in the glow discharge plasma. Strong absorption saturation was observed at high laser intensity. Absorption saturation was also observed for other lines and in the microwave discharge plasma. The Voigt parameter α of the measured profiles was kept less than 0.07 and then Doppler dominant approximation was valid for all conditions.

Figure 5 shows a plot of absorption coefficient and a theoretical curve-fitting of Eq.(18) as a function of I/I_{S_inhomo}, where I_{S_inhomo} was a fitting parameter. Figure 6 shows plots of $\Delta\nu_D$ and T. $\Delta\nu_D$ increased with I in contradiction to the conventional theory, resulting in the increase in T with I.

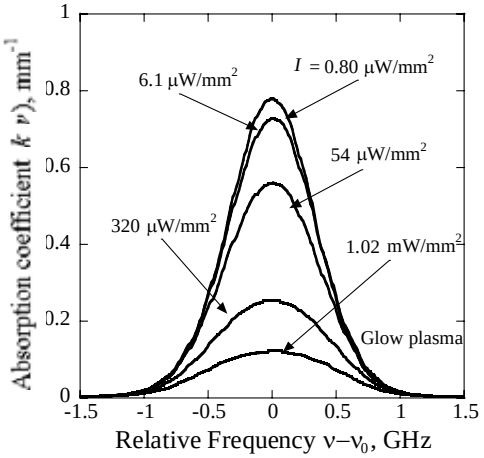

Figure 4. Variation of absorption profiles in the glow discharge argon plasma. ν_0 = 842.46 nm.

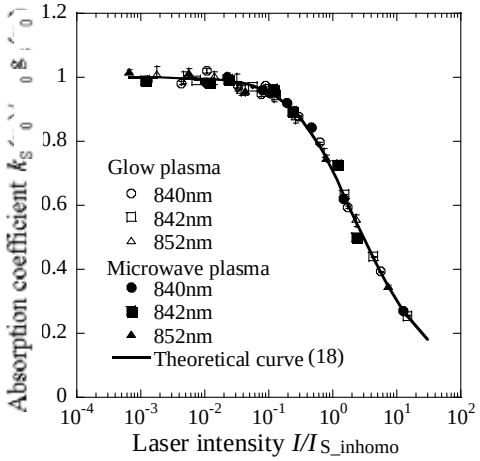

Figure 5. Relationship between absorption coefficient and laser intensity.

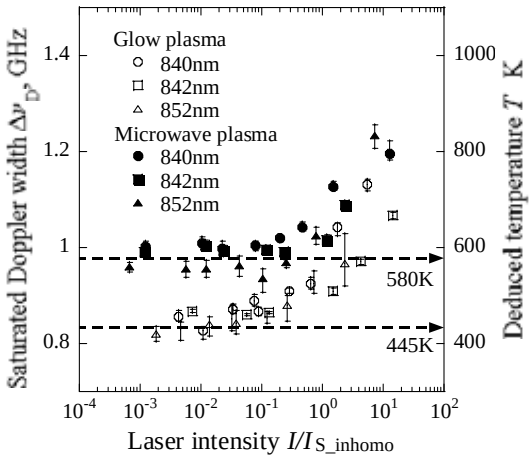

Figure 6. Saturated Doppler width and deduced tempearture.

4. Discussion

Dependency of I_{S_inhomo} on the Frequency

The experimental result suggests that I_{S_inhomo} should vary with the relative frequency $|\nu-\nu_0|$. The averaged velocity v seen in Eq. (19) may be a function of $|\nu-\nu_0|$. In fact, absorbers showing larger Doppler shift have higher averaged velocity: In the gas isotropic in a three-dimensional velocity field, velocity $v(\nu)$ averaged over the absorbers showing the Doppler shift $|\nu-\nu_0|$ is expressed as

$$v(\nu)=\sqrt{(\nu-\nu_0)^2\frac{c^2}{\nu_0^2}+\frac{2k_BT_0}{m}}=\bar{v}\sqrt{\frac{8\ln 2}{3}\frac{(\nu-\nu_0)^2}{\Delta\nu_D^2}+\frac{2}{3}} \quad . \tag{22}$$

Here, T_0 is the true temperature and . Assuming s is constant, I_{S_inhomo} is expressed as a function of ν by substituting Eq.(22) into Eq. (19),

$$I_{S\_inhomo}(\nu)=I_{S\_inhomo}\sqrt{\frac{8\ln 2}{3}\frac{(\nu-\nu_0)^2}{\Delta\nu_D^2}+\frac{2}{3}} \quad . \tag{23}$$

Figure 7 shows the theoretical plot of $I_{S\_inhomo}(\nu)/I_{S\_inhomo}$. $I_{S\_inhomo}(\nu_0 \pm\Delta\nu_D)$ is almost double of $I_{S\_inhomo}(\nu_0)$.

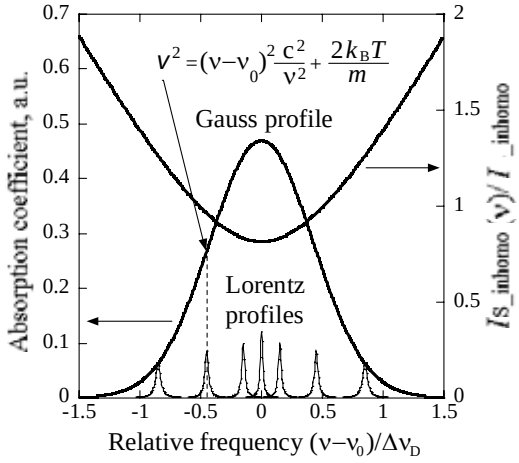

Figure 7. $I_{s\_inhomo}(\nu)/I_{s\_inhomo}$ and absorption profile.

Computed Profile and True Temperature

Figure 8 shows computed absorption profiles and a plot of relationship between computed absorption coefficient. Strong saturation effects are also observed in the computed absorption profiles and their coefficients are well fitted on the curve.

Figure 9 shows the FWHM of absorption profiles measured and computed from Eqs. (18) and (23). The results show a good agreement.

The ratio of deduced temperature to the true temperature is computed for various laser intensities and Voigt parameters as tabulated in Table 3. When probe laser intensity is high ($I/I_{S\_inhomo}>10^{-1}$), temperature will be overestimated and should be corrected by the factor shown in Table 3.

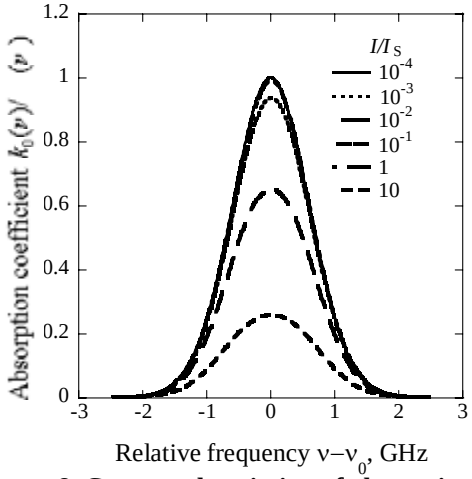

Figure 8. Computed variation of absorption profiles.

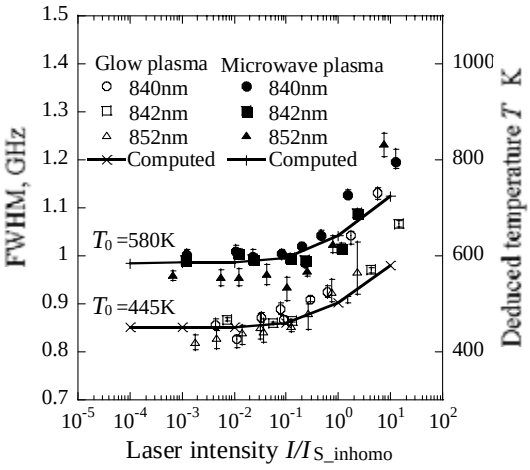

Figure 9. Measured and computed FWHM.

Table 3 Ratio of deduced temperature to true one T/T_0.

$\alpha(\nu_0)$	I/I_{S_inhomo}					
	10^{-4}	$10^{-4.}$	10^{-2}	10^{-1}	1	10
0.01	0.999	0.999	1.004.	1.018	1.107	1.216
0.05	1.014.	1.014.	1.014.	1.04.4.	1.14.8	1.4.41
0.1	1.04.7	1.04.7	1.04.7	1.057	1.189	1.585

A. Summary

Error and applicable limit of LAS are investigated. The fractional absorption more than 1% is measured within 1% error with measurement error of 10^{-2} %. An influence of this error on translational temperature measurements is also estimated. As a result, translational temperature is measured with in 5 % error for fractional absorption more than 10^{-2} with measurement error of 10^{-2} %. Then, in OI 777.19 nm measurements, the number density at least more than 10^{15} m^{-3} is necessary for temperature measurements within 5% error.

When probe laser intensity I is higher, Doppler broadening of absorption line becomes wider, and the temperature deduced from the broadening was found to tend to be overestimated in contradiction to the conventional laser theory.

This result is caused by the dependency of saturation intensity I_{S_inhomo} on the frequency: Absorbers showing larger Doppler shift $|\nu-\nu_0|$ have higher averaged velocity, and then increases with relative frequency $|\nu-\nu_0|$.

Even though probe laser intensity is high and saturation effect is large, true temperature can be obtained using a correction factor presented in this study.

I. Application to Arc-heater Plume [26-28]

A. Arc-heater

1. JUTEM Arc-heater

The schematic of the constricted type arc-heater developed at the Japan Ultra-high Temperature Materials Research Center (JUTEM) is shown in Fig.10. As seen in this figure, inert gas (argon is used in this experiment) is supplied from the base of cathode rod and oxygen is added at the constrictor part to prevent the cathode from oxidization.Diameter of constrictor is 4 mm. The flow Mach number is designed at 3. The input power, gas flow rates, specific enthalpy and ambient pressure were 7.2 kW, argon 20 slm, oxygen 5 slm, 6.1 MJ/kg and 38 Pa, respectively. A target line is the absorption from meta-stable atomic oxygen at 777.19 nm.

2. The University of Tokyo Arc-heater

The schematic of the constricted type arc-heater developed at the University of Tokyo is shown in Fig.11. Oxygen is injected at the constrictor part as described above. The flow Mach number of the plume was designed at 2. The thermal efficiency was estimated about 60% by measuring the increase in cooling water temperature. The input power, gas flow rates, specific enthalpy and ambient pressure were 1.1 kW, argon 6slm, oxygen 1 slm, 3.6 MJ/kg and 53 Pa, respectively. In addition to the OI 777.19 nm line, the ArI 8420.82 nm line is also targeted.

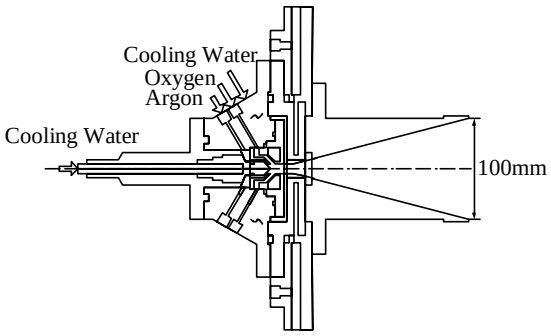

Figure 10. Schematic of JUTEM arc-heater.

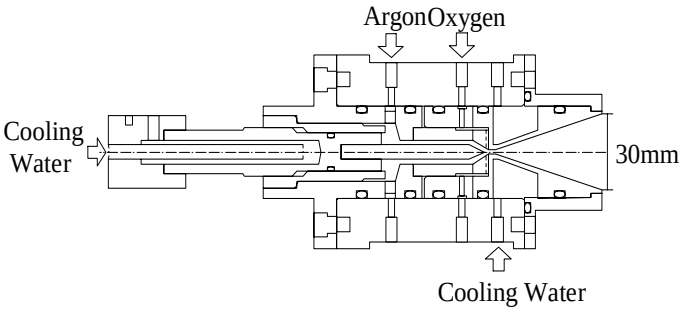

Figure 11. Schematic of University of Tokyo arc-heater.

B. Measured Results

Figure 12 shows the distributions of meta-stable oxygen number. At z=100 mm, the number density profile has two peaks at r=20 mm (here, z and r are defined by cylindrical coordinate and origin is taken at the center of nozzle exit). Then, these two peaks approach to the centerline in the downstream of the plume and combine at z=24.0 mm. The maximum number density is 3.1×10^{16} m^{-3}.

Figure 13 shows the distributions of meta-stable oxygen number. The profile of number density distribution is similar to that in Fig.12. That is, at z=0mm, the number density profile has a peak at r=11mm. Then, the peak approach to the centerline in the downstream of the plume and combine at z=60 mm. The maximum number density is 3.5×10^{16} m^{-3}.

Figure 14 shows the distributions of meta-stable argon number. Number density decreases monotonously along the centerline. The maximum number density is 3.0×10^{17} m^{-3}.

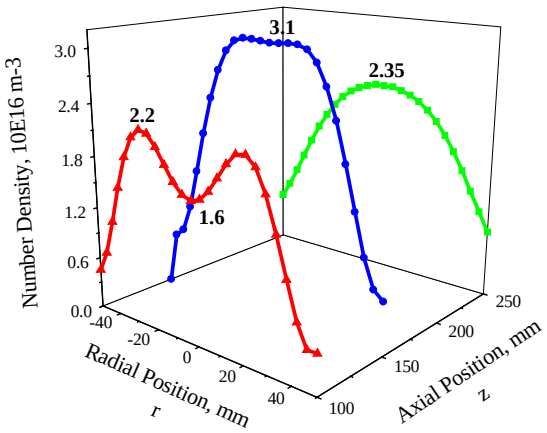

Figure 12. Number density distributions of atomic meta-stable oxygen in JUTEM Erosion Testing Machine.

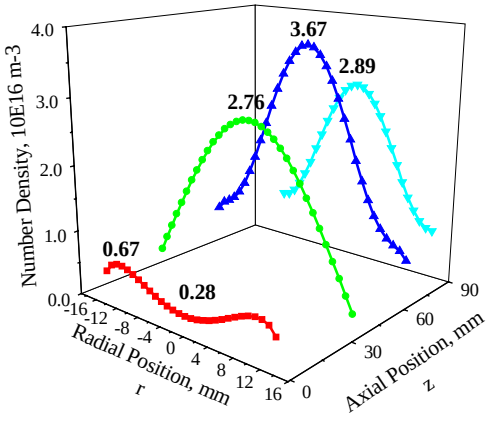

Figure 13. Number density distributions of atomic meta-stable oxygen in University of Tokyo arc-heater plumes.

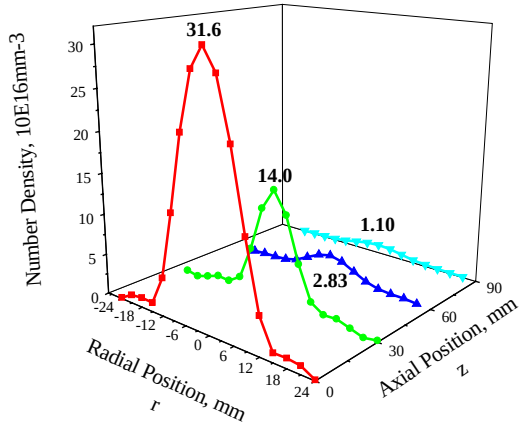

Figure 14. Number density distributions of atomic meta-stable argon in the University of Tokyo arc-heater plumes.

C. Discussion

The density peaks of meta-stable atomic oxygen were located off-axis at the nozzle exit and approached to the centerline as shown in Figs 12 and 13. Although the profile of ground state would be somehow different from that of meta-stable state, this result implies the following mixing process. Oxygen injected at the constrictor is not enough mixed with nitrogen in the nozzle. Then, oxygen diffuses from outside toward the centerline, being dissociated in the plume out of the nozzle. Since, oxygen does not pass through the high temperature cathode-jet region, degree of dissociation is unexpectedly small. The visualized schematic of mixing process is shown in Fig. 15.

In Fig.13, two density peaks located off-axis combine earlier than in Fig.12. This is partly because the size of the University of Tokyo's arc-heater is smaller than JUTEM's and the shear in the free jet is stronger resulting in larger turbulent

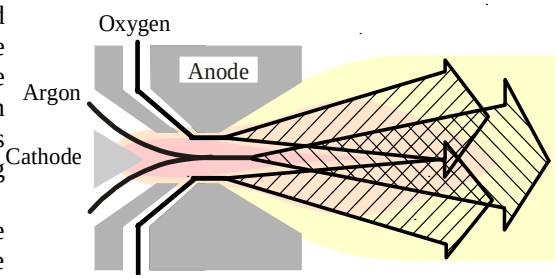

Figure 15. Mixing process.

transport, and partly because the flow Mach number of former plume is smaller than the latter one.

In the downstream, number density of meta-stable atomic oxygen is increasing, while that of meta-stable argon is decreasing as shown in Figs. 13 and 14. This is because oxygen is being dissociated in the plume, while meta-stable argon is being deexcited by collision and radiation.

D. Comparison with CFD results

For the comparison, CFD analysis was also conducted. The calculation model [26] is 1) 1-T model, 2) chemical nonequilibrium and seven chemical reaction processes, 3) Plandtl turbulent model and the computational mesh is shown in Fig.16. The results are shown in Figs. 17 18, and 19. As a result, the number density distribution has two peaks located off axis near the nozzle exit. Then, they these two peaks approach to the centerline and combine in the downstream of the plume. This result supports our predicted mixing process.

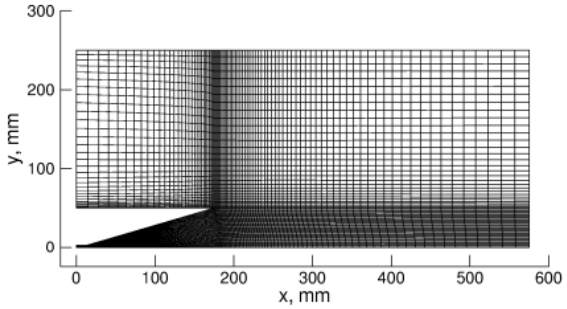

Figure 16. Computational mesh.

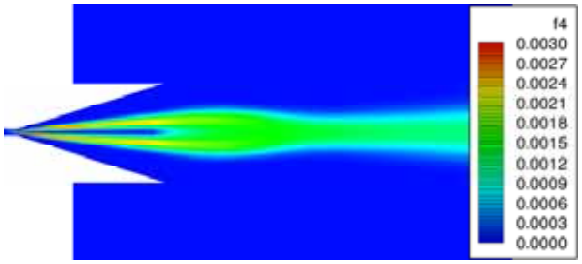

Figure 17. Mole fraction of atomic oxygen in the University of Tokyo arc-heater plume.

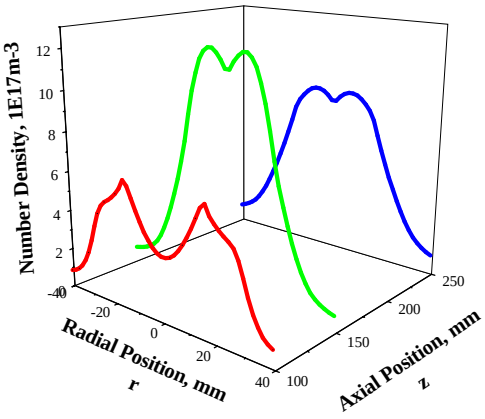

Figure 18. Number density distributions of atomic meta-stable oxygen simulated for University of Tokyo arc-heater plume.

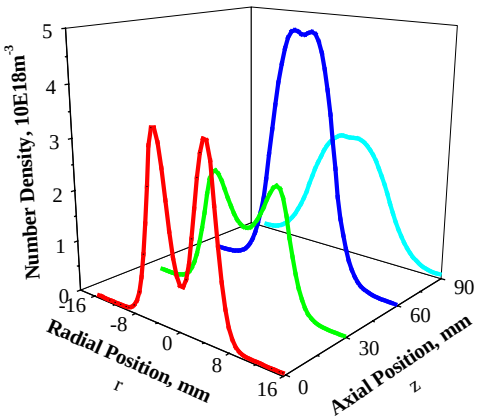

Figure 19. Number density distributions of atomic meta-stable oxygen simulated for University of Tokyo arc-heater plume.

E. Summary

Laser absorption spectroscopy was applied to the measurement of the two kinds of constricted arc plasma wind tunnel flows.

Number density distributions of atomic meta-stable oxygen were obtained from the measured absorption line profile at 777.19 nm in argon-oxygen plumes generated by arcjet type arc-heaters.

As a result, it was found that the oxygen is localized off axis at the nozzle exit, and diffuses from outside toward the centerline in the plume.

Moreover, numerical simulation was conducted to investigate the diffusion process of the oxygen in the arc-heater. The result indicates that the maximum degree of oxygen dissociation would be at the level of 0.01%.

II. Application to ICP Plume [29-31]

A. PWK3 System

A plasma wind tunnel (PWK3) including an inductively heated plasma generator (IPG3) has been developed at IRS, Stuttgart University [32-35]. A schematic of PWK3 is shown in Fig. 20. The size of the vacuum chamber is 2 m in length and 1.6m in diameter. The maximum pumping power of the vacuum system is up to 250000 m^3/h at 10 Pa, which corresponds to the pressure at the altitude of 90 km.

In IPG3, a Meissner type resonant circuit is used as a RF oscillator. Its operational frequency can be optimized to achieve high energy coupling efficiency for various gas species by changing the capacitance (6 nF~42 nF) as well as changing a coil, as shown in Fig.20. The range of the frequency in this circuit is from 0.5 MHz to 1.6 MHz.

A schematic of IPG3 is shown in Fig.21. IPG3 consists of an induction coil, a quarts tube containing plasma and a gas injection head. The induction coil made of copper has 5 turn with its inductivity of 2 μH. Both the induction coil and quartz tube are surrounded by an external tube and cooled to protect the tube from overheating. Various gases can be injected with swirl to stabilize the plasma.

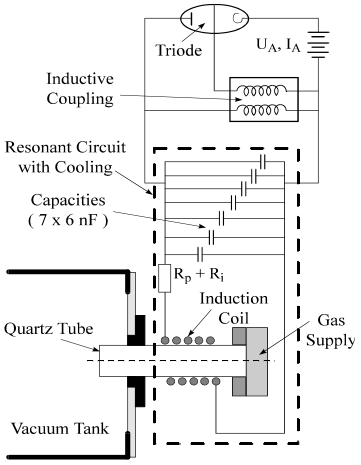

Figure 20. Schematic of Meissner type resonant circuit.

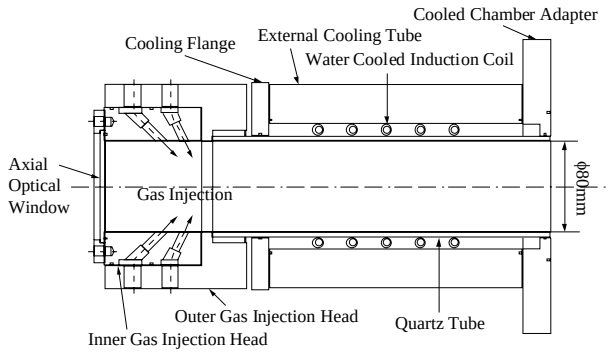

Figure 21. Schematic of IPG3.

B. Test Conditions and Previous Tests

Various intrusive measurements using a calorimeter, Pitot probe, Mach probe, and heat flux probe have been applied to the flows[35]. The operational condition and measured parameters by these methods are tabulated in Tables 4 and 5, respectively.

Figure 22 shows that the induction current has a specific characteristic. A plasma emission signal measured by a photo detector is also plotted in the figure. Both signals fluctuate at 300 Hz. This fact implies that the flow generated by IPG3 is not stationary.

Figure 23 shows that the measured region was $0<r<r_{max}$ at 130 mm downstream from the generator exit. Axisymmetric distributions of flow properties were assumed here; r represents the radial coordinate. In this experiment, rmax was set at 50 mm, which is equal to the generator exit radius. The test condition of IPG3 in LAS measurements is also the same with previous tests as shown in Table 4.

Table 4 Operational conditions.

Operational condition	Value
Working gas	O_2
Mass flow	3 g/s
Anode Power P_{anode}	110 kW
Coil turn	5.5
Number of capacitors	4
Chamber ambient pressure p_{amb}	30 Pa

Table 5 Measured parameters [35].

Parameter	Value
Plasma power P_{plasma}	28.2 kW
Total pressure p_0	410 Pa
Mach number M	3
Heat flux density q	2.1 MW/m^2

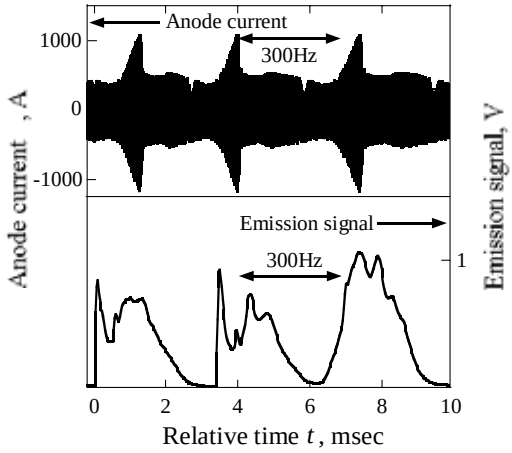

Figure 22. Induction current and plasma emission signal.

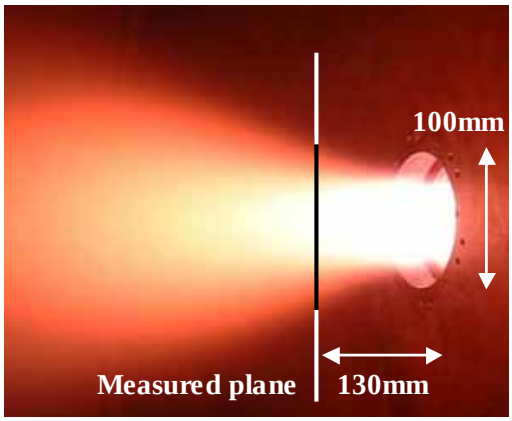

Figure 23. Photo of IPG3.

C. Results

Figure 24 shows the history of an absorption signal at the fixed laser frequency along with an emission signal. The absorption signal fluctuated in synchronization with the emission signal with a period t of 3.3 ms. Although the absorption signal decreases every 3.3 ms, it sometimes goes to zero and sometimes not. The signal traces can be categorized into two modes: in Mode 1, the trace starts from zero absorption condition, in which plasma has been distinguished for some time; in Mode 2, the trace starts increasing from non-zero absorption condition, in which plasma is sustained even at the minimum energy input.

Typical signals that were recorded with frequency modulation are shown in Fig. 25 along with an etalon signal. We recorded 40 cycles of frequency modulation for each measurement position. Absorption coefficients are extracted every 0.4 ms and rearranged according to elapsed time t and the modes. Thereby, we obtained an instantaneous absorption profile. Figure 26 shows typical absorption coefficients that were extracted from the absorption signal. Here, the origin of time, τ=0, is set at the minimum signal in each cycle.

Figure 27 shows instantaneous absorption profiles that were reconstructed through Abel inversion. Figure 28 shows that the history of T, as deduced from line broadening, was very similar to that of the emission signal. Here, T at τ=0 in Mode 2 was set at 75 K, assuming isentropic expansion of cold gas from the generator. The maximum temperature was 9500 K.

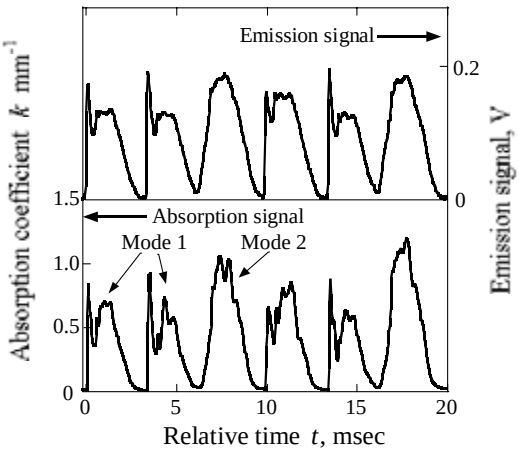

Figure 24. Absorption signal at $\nu=\nu_0$ – 4 GHz and emission signal, r=0 mm.

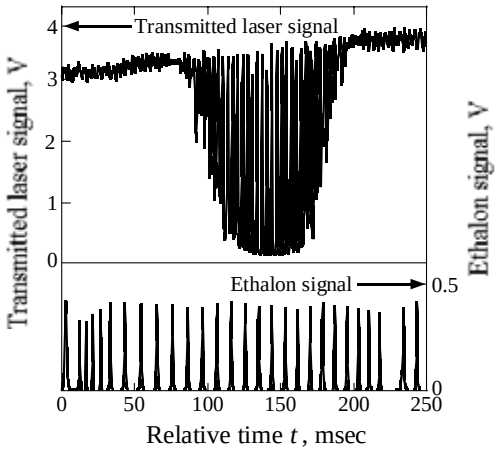

Figure 25. Typical transmitted laser and etalon signals, *r*=0 mm.

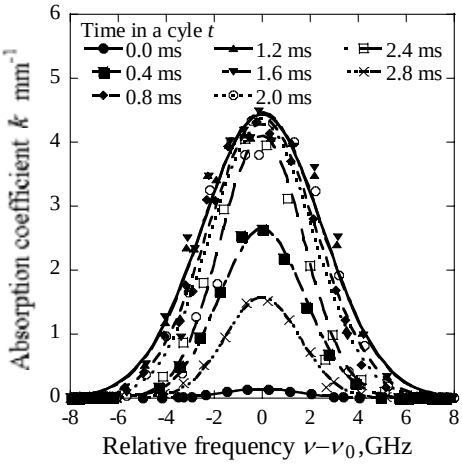

Figure 27. Temporal variations of absorption profile in Mode 1, *r*=0 mm.

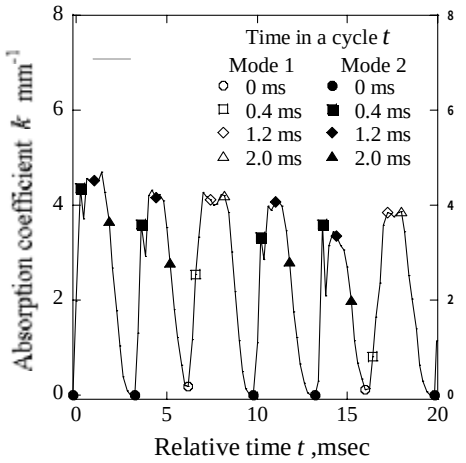

Figure 26. Typical absorption coefficient and extracted one in each cycle, *r*=0 mm.

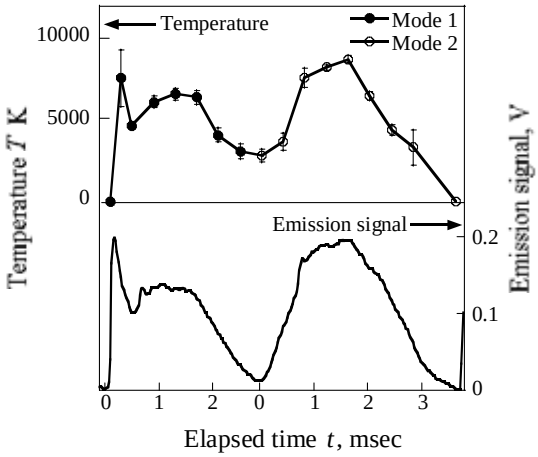

Figure 28. History of translational temperature and emission signal, *r*=0 mm.

D. Discussion

1. Temporal Variation of Plasma Properties

The specific total enthalpy, h_0, is the sum of static enthalpy CpT, chemical potential h_{chem} and kinetic energy $u^2/2$, expressed as

$$h_0 = C_p T + h_{chem} + \frac{1}{2}u^2 \tag{24}$$

Here, C_p is the specific heat at constant pressure and u is the flow velocity expressed as

$$u = M\sqrt{\gamma RT} \tag{25}$$

Here, γ and R are the specific heat ratio and the gas constant, respectively.

Thermo-chemical equilibrium is assumed for simplicity and we estimate h_0 and mole fractions from the measured T. Three chemical species, O_2, O, and O+, and two chemical reactions $O_2 \rightarrow 2O$ and $O \rightarrow O^+ + e^-$ are

considered. Their equilibrium constants were obtained from Ref. 36. *C*p is computed as the sum of the contributions of each species. Figure 29 shows calculated equilibrium properties at p_{amb}=30 Pa.

Figure 30 shows the history of estimated properties on the plume axis. Maximum h_0 was 86 MJ/kg and the averaged degree of dissociation of oxygen is 0.83. At the highest enthalpy, the mole fraction was 0.7 because of ionization. Its degree of dissociation was very high. For that reason, it would be useful for precise evaluation of catalytic effects for various TPS materials.

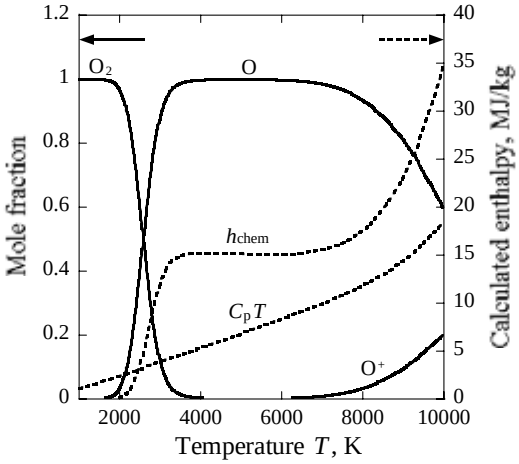

Figure 29. Calculated enthalpy and mole fractions, p_{amb}=30 Pa.

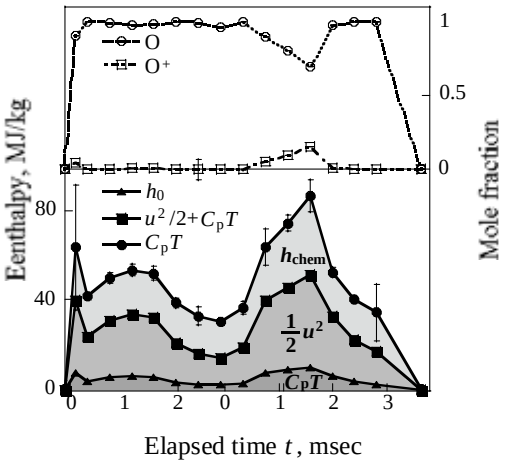

Figure 30. History of estimated enthalpy and mole fractions, r=0 mm.

2. *Time Averaged Specific Total Enthalpy*

The time-averaged specific total enthalpy $\bar{h}_0(r)$ is defined as

$$\bar{h}_0(r) = \frac{\int_0^{\tau} h_0(r,t)\rho(r,t)u(r,t)\mathrm{d}t}{\int_0^{\tau} \rho(r,t)u(r,t)\mathrm{d}t} \tag{26}$$

where $\rho(r,t) = p_{amb}/k_B T(r,t)$.

Figure 31 shows the distribution of $\bar{h}_0(r)$ with that estimated from the probe measurements described next section. Although it took a maximum of 33.7±2.9 MJ/kg on the axis, the profile was almost flat for the TPS probe area (r<10.5 mm). Figure 32 shows the enthalpy balance at r=0, where $\bar{h}_{chem}$ accounted for 42.5% of $\bar{h}_0(r)$.

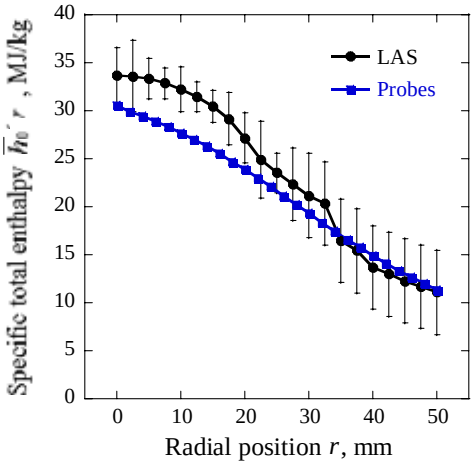

Figure 31. Time-averaged specific total enthalpy distribution by LAS and Probes.

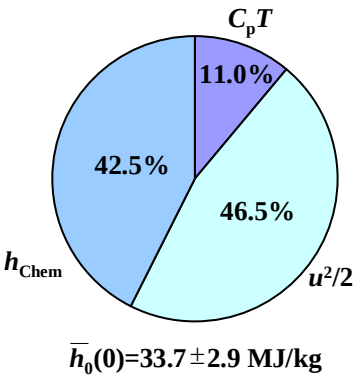

Figure 32. Enthalpy balance, *r*=0 mm.

3. Comparison with Intrusive Measurements

Plasma power P_{plasma}, $r<r_{\max}$ and the mass flow rate $\dot{m}$ $r<r_{\max}$ contained in the measured cylinder of the flow are obtained as

$$P_{\text{plasma},\, r<r_{\max}} = \int_0^{r_{\max}} 2\pi r \rho(r) u(r) \bar{h}_0(r)\, dr \tag{27}$$

$$\dot{m}_{r<r_{\max}} = \int_0^{r_{\max}} 2\pi r \rho(r) u(r)\, dr \tag{28}$$

Table 6 shows those results in comparison with the calorimeter measurements. Figure 23 shows that P_{plasma}, $r<r_{\max}$ in LAS is smaller than those of calorimeter measurements16 because the flow has expanded to the region of $r>r_{\max}$.

Table 6 Comparison of P_{plasma}

Method	$r_{\max}$	P_{plasma}
LAS (Present)	50 mm	17.5 kW
Calorimeter22	60 mm	28.2 kW

In Ref. 35, $\bar{h}_0(r)$ was estimated from the measured $\dot{q}(r)$, $p_0(r)$, and P_{plasma} using Pope's relation as [37],

$$\bar{h}_0(r) = \frac{r_{\max}^2}{2} \frac{\dot{q}(r)/\sqrt{p_0(r)}}{\int_0^{r_{\max}} \left(\dot{q}(r)/\sqrt{p_0(r)}\right) r dr} \frac{P_{\text{plasma},\, r<r_{\max}}}{\dot{m}_{r<r_{\max}}} \tag{29}$$

Here, $\dot{m}_{r<r\max}$= $\dot{m}$ =3g/s was assumed regardless $r_{\max}$=60 mm. Table 7 shows a comparison between intrusive measurements and present study. Results show good agreement. The values would more closely resemble one another than those in Table 5-4 if $\dot{m}_{r<r\max}$ is estimated precisely in intrusive measurements.

Table 7 Comparison of $\bar{h}_0$ (0)

Method	$\bar{h}_0(0)$
LAS (Present)	33.7±2.9 MJ/kg
Intrusive measurements22	30.5 MJ/kg

E. Summary

Laser absorption spectroscopy was applied for the diagnostics of IPG3 pure oxygen flow. The flows were non-stationary and its emission and absorption signals were found to fluctuate at 300 Hz because of the fluctuation of anode power.

Then, temporal and spatial translational temperature distributions were measured. The maximum temperature was found to be 9000 K instantaneously.

The corresponding averaged degree of dissociation of oxygen estimated by the measured temperature and thermo-chemical equilibrium calculation is more than 0.90. The total enthalpy was estimated as 33.7±2.9 MJ/kg; 43% of it was possessed as the chemical potential. These results show good agreement with intrusive measurements.

III. Conclusion

A diode laser absorption spectroscopy system applicable to low-pressure plasma has been successfully developed with following remarks.

A. Development of LAS system

1. Error analysis

Relationship of errors between translational temperature and measured fractional absorption were analytically investigated. As a result, translational temperature is estimated with in 5 % error for fractional absorption more than 10^{-2} with its measurement error of 10^{-2} %. This fractional absorption requires number density more than 10^{15} m^{-3} in OI 777.19 nm line with 1cm optical path.

2. Absorption saturation

When probe laser intensity I is higher, strong absorption saturation was observed. As a result, absorption coefficients were found to decrease with laser intensity according to the conventional laser theory. Then, number density should be estimated using the theory.

On the other hand, Doppler broadening of absorption line becomes wider with laser intensity, and the temperature deduced from the broadening tends to be overestimated in contradiction to the theory. This result is caused by the dependency of saturation intensity I_{S_inhomo} on the frequency: Absorbers showing larger Doppler shift $|\nu-\nu_0|$ have higher averaged velocity, and then increases with relative frequency $|\nu-\nu_0|$.

Therefore, in case of $I/I_{S\_inhomo} > 10^{-1}$, where strong laser intensity is necessary due to strong plasma emission, measured temperature should be calibrated by the correction factor presented in this paper, though in case of $I/I_{S\_inhomo} > 10^{-1}$, temperature is precisely measured.

B. Application to Plasma Wind Tunnel Flows

Next, this system was applied to two kinds of plasma wind tunnel flows and various properties of the flows were successfully clarified. Also portability of this system is proved by measurements in other facilities in Japan and Germany.

1. Constricted arc heater flows: mixing process of oxygen

Oxygen injected at the constrictor was found not enough mixed with argon base flow at the nozzle exit. The oxygen slowly diffused toward the axis in the downstream region of the plume, resulting in the quite small degree of dissociation of oxygen at the level of 0.01%. For the enhancement of the oxygen dissociation, the oxygen injection method should be improved to promote the mixing between oxygen and argon.

2. ICP flows: Temperature measurements and enthalpy estimation

Laser absorption spectroscopy was successfully applied for the diagnostics of non-stationary IPG3 flow. Consequently, the averaged degree of dissociation of oxygen is more than 0.92. The total enthalpy was estimated as 33.7±2.9 MJ/kg; 43% of it was possessed as the chemical potential. These results show good agreement with intrusive measurements.

Acknowledgments

The work has been supported by Research Fellowships of the Japan Society for the Promotion of Science for Young Scientists.

References

[1]Bertin, J. J., "Hypersonic Aerothermodynamics," AIAA Education Series, AIAA, Inc., Washington, DC, 1994

[2]Throckmorton, D. A., "Shuttle Entry Aerothermodynamic Flight Research: The Orbiter Experiments Program," *Journal of Spacecraft and Rockets*, Vol. 30, No. 4, 1993, pp. 449-465.

[3]Gnoffo, P. A., Braun, R. D, Weilmuenster, K. J., Mitcheltree, R. A., Engelund, W. C., and Powell, R. W., "Prediction and Validatin of Mars Pathfinder Hypersonic Aerodynamic Data Base," AIAA Paper 98-2445, June 1998.

[4]Seiff, A., Kirk, D. B., Young, R. E., Blanchard, R. C., Findlay, J. T., Kelly, G. M., and Sommer, S. C., "Measurement of Thermal Structure and Thermal Contrasts in the Atmosphere of Venus and Related Dynamical Observations: Results from the Four Pioneer Venus Probes," Journal fo Geophysical Research, Vol. 85, NO. A13, 1980, pp. 7903-7933.

[5]Tauber, M., Wercinski, P., Henline, W., Paterson, J., and Yang, L., "Uranus and Neptune Atmospheric-Entry Probe Study," Journal of Spacecraft and Rockets, Vol. 31, No. 5, 1994, pp. 799-805.

[6]Auweter-Kurtz, M., "Overview of IRS Plasma Wind Tunnel Facilities," Measurement Techniques for High Enthalpy and Plasma Flows, NATO Research and Technology Organization proceedings RTO-EN-8, Neuilly-Sur-Seine Cedex, France, 2000, pp. 2A-1-1A-20.

[7]Anfimov, N., "TSNIIMASH Capabilities for Aerogasdynamical and Thermal Testing of Hypersonic Vehicles," AIAA Paper 92-3962, June 1992.
[8]Balter-Peterson, A., Nichols, F., Mifsud, B., and Love, W., "Arcjet Testing in NASA Ames Research Center Thermophysics Facilities," AIAA Paper 92-1071, 1992
[9]Smith, R. K., Wagner, D. A., and Cunningham, J. W., "A Survey of Current and Future Plasma Arc-heated Test Facilities for Aerospace and Commercial Applications," AIAA Paper 98-0146, Jan. 1998.
[10]Sharma, S. P., "Research on Nonequilibrium Phenomena at Ames E.A.S.T. Facility," 19th International Symposium on Shock Waves, 1993.
[11]Storm, P. V. and Cappelli, M. A., "Laser-induced fluorescence measurements within an arcjet thruser nozzle," AIAA Paper 95-2381, July 1995.
[12]Winter, M. W. and Auweter-Kurtz, M., "Boundary layer investigation in front of a blunt body in a subsonic air plasma flow by emission spectroscopic means," AIAA paper 98-2460, 1998.
[13]Sharma, S. P., Park, C., Scott, C. D., Arepalli, S., and Taunk, J., "Arcjet Flow Characterization," AIAA Paper 96-0612, 1996.
[14]Scott, C. D., "Effects of Nonequilibrium and Wall Catalysis on Shuttle Heat Transfer," *Journal of Spacecraft*, Vol. 22, No. 5, 1985, pp.489-499.
[15]Chen, Y. K. and Milos, F. S., "Ablation and Thermal Response Program for Spacecraft Heatshield Analysis," *Journal of Spacecraft and Rockets*, Vol. 36, No. 3, 1999, pp. 475-483.
[16]Armenise, I., Barbato, M., Capitelli, M. and Gorse, C., "Surface Recombination Coefficients and Boundary-Layer Hypersonic Flow Calculations on Different Surfaces," Journal of Spacecraft and Rockets, Vol. 41, No. 2, 2004, pp. 310-313.
[17]Laux, T., Feigl, M., Auweter-Kurtz, M., Stockle, T., "Estimation of Surface Catalytcity of PVD-Coatings by Simultaneous Heat Flux and LIF Measurements in High Enthalpy Air Flows," AIAA Paper 00-2364, 2000.
[18]Demtroder, W., "Laser Spectroscopy," second ed., Berlin, Springer Verlag, 1996.
[19]Baer D. S., and Hanson, R. K., "Tunable Diode Laser Absorption Diagnostics for Atmospheric Pressure Plasmas," *Journal of Quantive Spectroscopy and Radiative Transfer* Vol. 47, 1992, pp. 455-475.
[20]Kim., S., "Development of Tunable Diode Laser Absorption Sensors for A Large-Scale Arc-Heated-Plasma Wind Tunnel," Doctor thesis, Stanford University, 2004.
[21]Herzberg, G., "Atomic spectra and atomic structure, Dover Publications," New York, 1944.
[22]Griem, H. R., "Plasma Spectroscopy," McGraw-Hill, Inc., 1964.
[23]NIST Atomic Spectra Database, http://physics.nist.gov/cgi-bin/AtData/main_asd
[24]Matsui, M., Satoshi, O., Komurasaki, K., and Arakawa, Y., "Translational Temperature Measurement of Arc-heater Pumes by a Laser Absorption Spectroscopy," 41st AIAA Aerospace Sciences Meeting and Exhibit, AIAA Paper 03-0587, 2003.
[25]Matsui, M., Komurasaki, K., and Arakawa, Y., "Absorption Saturation in Laser Absorption Spectroscopy," 24th AIAA Aerodynamic Measurement Technology and Ground Testing Conference, AIAA Paper 04-2597, 2004.
[26]Matsui, M., Takayanagi, H., Oda, Y., Komurasaki, K., Arakawa, Y., "Performance of arcjet-type atomic-oxygen generator by laser absorption spectroscopy and CFD analysis," *Vacuum*, Vol.73, 3-4, 2004, pp.341-346.
[27]Matsui, M., Komurasaki, K., Arakawa, Y., "Characterization of Arcjet Type Arc-Heater Plumes, "AIAA 02-2242, 2002.
[28]Matsui, M., Ogawa, S., Oda, Y., Yamaji, I., Komurasaki, K., and Arakawa, Y., "Concentration of Atomic Oxygen in Arc-heater Simulators," 3rd Atmospheric Reentry vehicles and systems symposium, 2003.
[29]Matsui, M., Herdrich, G., Komurasaki, K., and Auweter-Kurtz, M., "Combined Laser Absorption Spectroscopy and Probe Measurements in Inductively Heated High Enthalpy Plasmas," 36th AIAA Thermophysics Conference, AIAA Paper 03-3892, 2003.
[30]Matsui, M., Herdrich, G., Komurasaki, K., and Auweter-Kurtz, M., "Laser Absorption Spectroscopy in Inductive Plasma Generator Flows," 42nd AIAA Aerospace Sciences Meeting and Exhibit, AIAA Paper 04-1222, 2004.
[31]Matsui, M., Komurasaki, K., Herdrich, G., and Auweter-Kurtz, M., "Temporally Resolved Measurement of Enthalpy in Inductively Heated Plasma Generator Flows," 4th Atmospheric Reentry vehicles and systems symposium, 2005.
[32]Herdrich, G., Auweter-Kurtz, M., and Kurtz, H., "New Inductively Heated Plasma Source for Reentry Simulations," *Journal of Thermophysics and Heat Transfer*, Vol. 14, No. 2, 2000, pp. 244-249.
[33]Herdrich, G., Auweter-Kurtz M., Endlich, P. and Kurtz, H., "Mars Entry Simulation Using an Inductively Heated Plasma Generator," *Journal of Spacecraft and Rocket*, Vol. 40, No. 5, 2003, pp. 690-693.
[34]Herdrich, G., Auweter-Kurtz, M. and Kurtz, H., "A new inductively heated plasma source for re-entry simulations," AIAA Paper 98-3022, 1998.
[35] Herdrich, G. and Auweter-Kurtz, M., "Development and Characterization of Inductively Heated Plasma Generator for Atmospheric Entry Simulations," AIAA Paper 04-2503, Jun. 2004.
[36]Guputa, R. N., Yos, J. M., Thompson, R. A., and Lee, K. P., "A Review of Reaction Rates and Thermodynamic and Transport Properties for an 11-Species Air Model for Chemical and Thermal Nonequilibrium Calculations to 30000K," NASA Reference Publication 1232, 1990.
[37]Marvin, J. G. and Pope, R.B., "Laminar Convective Heating and Ablation in the Mars Atmosphere," AIAA Journal, Vol. 5, No. 2, 1967, pp. 240–248.